

Binary nucleation kinetics. II. Numerical solution of the birth–death equations

Barbara E. Wyslouzil^{a)} and Gerald Wilemski^{b)}

Department of Chemical Engineering, Worcester Polytechnic Institute, Worcester, Massachusetts, 01609-2280; Lawrence Livermore National Laboratory, Livermore, California 94551-9900; and Physical Sciences Inc., Andover, Massachusetts 01810-1077

(Received 23 November 1994; accepted 22 February 1995)

We numerically solve the complete set of coupled differential equations describing transient binary nucleation kinetics for vapor-to-liquid phase transitions. We investigate binary systems displaying both positive and negative deviations from ideality in the liquid phase and obtain numerical solutions over a wide range of relative rates of monomer impingement. We emphasize systems and conditions that either have been or can be investigated experimentally. In almost every case, we find behavior consistent with Stauffer's idea that the major particle flux passes through the saddle point with an orientation angle that depends on the rates of monomer impingement. When this is true, the exact numerical steady state nucleation rates are within 10%–20% of the predictions of Stauffer's analytical theory. The predictions of Reiss' saddle point theory also agree with the numerical results over a wide range of relative monomer impingement rates as long as the equilibrium vapor pressures of the two pure components are similar, but Stauffer's theory is more generally valid. For systems with strong positive deviations from ideality, we find that the saddle point approximation can occasionally fail for vapor compositions that put the system on the verge of partial liquid phase miscibility. When this situation occurs for comparable monomer impingement rates, we show that the saddle point approximation can be rescued by evaluating an appropriately modified nucleation rate expression. When the two impingement rates differ significantly, however, the major particle flux may bypass the saddle point and cross a low ridge on the free energy surface. Even in these rare cases, the analytical saddle point result underpredicts the numerical result by less than a factor of 10. Finally, we study the transition from binary to unary nucleation by progressively lowering the vapor concentration of one component. Both Reiss' and Stauffer's rate expressions fail under these conditions, but our modified rate prescription remains within 10%–20% of the exact numerical rate. © 1995 American Institute of Physics.

I. INTRODUCTION

The direct numerical approach of solving the complete set of cluster birth and death equations is a useful way to study nucleation. The results let us evaluate the robustness of available steady state nucleation rate expressions as well as test the analytical approximations for time lags, or induction times, and transient particle formation rates. If analytical expressions fail, numerical results can help us determine why and to what degree. Numerical methods are essential for including effects not amenable to analytical treatment such as simultaneous cooling and nucleation in glasses¹ or heat transfer between clusters and the background gas during nucleation.² In binary nucleation the transition between binary and unary nucleation can be observed, and numerical results may reveal effects overlooked or poorly described by analytical treatments.

Recently, several investigators have studied binary nucleation by numerically solving the kinetics equations describing time dependent cluster formation. Nishioka and Fujita³ chose the H₂SO₄–H₂O system, but they were not able to follow the evolution of the equations to the steady state because the time lags in this system are much greater than

the times attainable by their computations (≈ 1 ms). Kožisek and Demo⁴ investigated both vapor–liquid and liquid–solid phase transitions. However, for the vapor–liquid example they only investigated the simple case of an extremely idealized mixture proposed by Temkin and Shevelev⁵ with no reference to an actual physical system. They found that their numerical results did not agree with the analytical theories of either Reiss⁶ or Stauffer,⁷ but for another set of calculations they did find good agreement with the Kelvin model of Temkin and Shevelev.⁵ Greer *et al.*⁸ found excellent agreement with the Reiss theory when the mobilities of the two species in the condensed phase were identical, but they observed that the major particle flux bypassed the saddle when the mobility of one of the species was decreased. In the latter case, the Reiss theory did not agree with the numerical results. No other quantitative comparisons were made. Very recently, McGraw⁹ applied matrix inversion techniques to solve the steady state binary kinetics equations. McGraw studied the H₂SO₄–H₂O system and included the effects of gas phase hydrates. He found quantitative agreement with the rate expression of Shugard, Heist, and Reiss¹⁰ (SHR) except at the extremely high water-to-acid impingement rate ratio $\approx 10^{14}$. Here the major flux bypassed the saddle, and the nucleation rate was enhanced by three orders of magnitude over the SHR value. Vehkamäki *et al.*¹¹ have also recently

^{a)}Present address: Worcester Polytechnic Institute.

^{b)}Present address: Lawrence Livermore National Laboratory.

reported using matrix methods to solve for the steady state rate.

In this paper we investigate steady state binary nucleation in the vapor phase by setting up and numerically solving the coupled differential equations governing the time evolution of the cluster population. A discussion of our transient results is deferred to a later paper.¹² One of our aims is to stringently test several analytical binary rate expressions by studying nucleation over a much larger range of conditions and for many more different types of systems than have previously been considered. Another goal is to develop a deeper appreciation for the relative importance of the many factors that affect the transient and steady state behavior of the nucleation fluxes on the free energy surface. These factors include the impingement rates, equilibrium vapor pressures, vapor phase activities, liquid molar volumes, and degree of mixture nonideality. In Sec. II we first present the kinetics equations and rate constants needed to solve these equations. We then discuss briefly how using a modified binary equilibrium distribution function and properly symmetrized impingement rate expressions ensures that the kinetics equations are fully self-consistent. After a brief description of our computational approach, we summarize the analytical binary nucleation rate expressions that we will use for comparison with our numerical results. In Sec. III we present and discuss our results. We first concentrate on detailed presentations of steady state behavior for several ideal and nonideal binary systems. Extensive comparisons with analytical results are made to establish the limits of validity of the following approximations and assumptions used in these theories: the saddle point flux assumption, the steepest descent approximation of Reiss, and the direction of principal growth approximation of Stauffer. In one of our cases, we present an explicit example of ridge crossing behavior in which the major nucleation current bypasses the saddle point. Next, we consider the transition from binary to unary nucleation by comparing numerical results with analytical predictions for a series of cases with progressively diminishing amounts of one vapor component. We rigorously test the capability of a modified version of a rate prescription¹³ designed to handle this transition. We conclude the paper with a summary and brief discussion of the steady state results in Sec. IV. Appendix A contains the derivation of the modified binary rate prescription. Appendix B contains the physical properties of the binary mixtures we considered.

II. BASIC EQUATIONS AND COMPUTATIONAL PROCEDURES

A. Kinetics equations

If growth and decay of clusters proceeds only by the addition or loss of monomers, the fluxes between adjacent cluster sizes, J_A and J_B , are determined by the differences between the forward and reverse rates for these processes,

$$J_A(i, j, t) = \Gamma_A(i, j) N_A f(i, j, t) - E_A(i+1, j) f(i+1, j, t), \quad (1)$$

$$J_B(i, j, t) = \Gamma_B(i, j) N_B f(i, j, t) - E_B(i, j+1) f(i, j+1, t). \quad (2)$$

In these equations, $\Gamma_\nu(i, j)$ is the rate coefficient for adding a monomer of type ν to a cluster containing i molecules of species A and j molecules of species B , $E_\nu(i, j)$ is the rate coefficient for removing a monomer of species ν from a cluster with composition (i, j) , and $f(i, j, t)$ is the nonequilibrium cluster concentration. The monomer concentrations are defined as $N_A = f(1, 0, t)$ and $N_B = f(0, 1, t)$. The evaporation rate coefficients depend on the composition of the cluster but should be independent of the gas phase composition and pressure. In this paper we do not account for surface enrichment of the clusters,^{14–16} and we calculate the evaporation rate coefficients based on the overall composition of the cluster rather than the thermodynamically correct *interior composition* of the cluster. For systems such as ours, where the surface tensions differ by, at most, 5%–15%, the overall and interior compositions will be almost identical.

The change in the number density of clusters of composition (i, j) with time is given by

$$\frac{df(i, j, t)}{dt} = J_A(i-1, j, t) - J_A(i, j, t) + J_B(i, j-1, t) - J_B(i, j, t), \quad (3)$$

except for the mixed dimer concentration. In this case, either $J_A(0, 1)$ or $J_B(1, 0)$ must be omitted from the right-hand-side to avoid doubling the mixed dimer flux because these two flux expressions are redundant. With constant monomer concentrations, there are $(i_{\max} \times j_{\max} - 3)$ coupled differential equations, where $i_{\max} - 1$ and $j_{\max} - 1$ are the maximum numbers of A and B molecules considered per cluster. Our solution procedure is described in Sec. II D.

B. The equilibrium distribution

The reverse rate coefficients required by the kinetics scheme are derived by applying the principal of detailed balance to Eqs. (1) and (2) together with prescriptions for the forward rate coefficients and the equilibrium distribution. There are difficulties associated with developing well-posed equilibrium distributions even in the case of unary nucleation.¹⁷ When the reversible work $W(g)$ required to form a cluster containing g molecules from the vapor is given by the capillarity approximation, issues of mass action and limiting consistency lead to a “self-consistent” form of the equilibrium distribution.¹⁸

As discussed in our previous paper (WWI),¹⁹ deriving a simple, self-consistent cluster distribution is more difficult in the case of binary nucleation, although the need for such a distribution was recognized 20 years ago.^{13,20} In particular, a well-posed binary cluster distribution should be dimensionally correct and of the same order of magnitude as other self-consistent classical distributions. It should satisfy the mass action law for chemical equilibrium, reduce to the self-consistent classical expression for one component, and revert to the equivalent single component value for the case of a degenerate isomeric mixture (i.e., when the properties of A = properties of B). Finally, evaporation rates derived from this binary distribution by detailed balancing should not depend on the monomer concentrations. The binary equilibrium distribution developed by Reiss,

$$N(i,j) = (N_A + N_B) \exp\left(\frac{-W(i,j)}{kT}\right), \quad (4)$$

does not meet several of these conditions, and, in fact, no previously published binary distribution satisfies all of these conditions. Even the solution recently suggested by Kulmala, Laaksonen, and Gershick²¹ fails the mass action test. In WWI we proposed¹⁹ the following self-consistent expression for the equilibrium binary cluster concentrations

$$N(i,j) = (N_A^\infty)^{x_A} (N_B^\infty)^{x_B} \times \exp(x_A \Theta_A + x_B \Theta_B) \exp\left(\frac{-W(i,j)}{kT}\right), \quad (5)$$

where N_ν^∞ are the monomer number densities in equilibrium with pure liquids of type ν , $x_A = 1 - x_B = i/(i+j)$, $\Theta_\nu = s_\nu \sigma_\nu / (kT)$, s_ν is the surface area of a monomer of type ν , σ_ν is the surface tension of pure liquid of type ν , k is the Boltzmann constant, and T is the temperature. For an ideal gas, the capillarity approximation for $W(i,j)$ gives

$$W(i,j) = -ikT \ln\left(\frac{N_A}{N_A^\infty(i,j)}\right) - jkT \ln\left(\frac{N_B}{N_B^\infty(i,j)}\right) + \Omega^s(i,j), \quad (6)$$

where $N_\nu^\infty(i,j)$ is the equilibrium number density of monomers of species ν in a saturated vapor over a bulk solution of composition x_A and $\Omega^s(i,j) = \sigma s(i,j)$, where the surface area of the cluster $s(i,j)$ and σ are also functions of composition. Although a binary cluster distribution based on either density functional calculations²² or Monte Carlo simulations²³ would be more satisfying, fundamental results of this type are not available for now. Our prescription enables us to carry out an internally consistent and numerically correct analysis whose results we can compare quantitatively with those from both binary and unary analytical nucleation rate expressions. We will refer to the distribution in Eq. (5) as the self-consistent classical (SCC) binary distribution. As in unary SCC theory, the effect of our binary SCC correction terms is to increase the concentrations of the clusters, usually by several orders of magnitude over the values given by Eq. (4).

C. Impingement and evaporation coefficients

Reiss' kinetic scheme⁶ provides a broadly acceptable conceptual basis for treating binary kinetics, but there are some symmetry problems that must be corrected if one wishes to find robust *numerical* solutions for the transient and steady state kinetics. This symmetry is important for getting the correct collision frequencies for small clusters and for avoiding spurious mass flows. The collision rate between an A and a B monomer obviously equals the collision rate between B and A , but the standard expression for the forward rate coefficient,

$$\Gamma_\nu = \pi d(i,j)^2 \sqrt{\frac{kT}{2\pi m_\nu}}, \quad (7)$$

where $d(i,j)$ is the diameter of the cluster and m_ν is the molecular mass of the impinging species, results in two different expressions for the forward rate of mixed dimer for-

mation. The solution is to use the simple expression for the collision frequency between two particles of unequal mass available from the kinetic theory of gases. This expression has been used in nucleation theory before when treating sulfuric acid hydrates.^{10,24} The corresponding forward rate coefficient then reads

$$\Gamma_\nu(i,j) = \pi [d_\nu + d(i,j)]^2 \sqrt{\frac{kT[m_\nu + m(i,j)]}{2\pi m_\nu m(i,j)}}, \quad (8)$$

where $m(i,j)$ is the molecular mass of the cluster. We will use this expression for all cluster sizes, although it reduces to the conventional expression for large enough values of i and j .

As discussed in WWI, the combination of our binary SCC equilibrium distribution and the symmetric impingement formula results in a unique value for every evaporation coefficient. The evaporation rate coefficients we used in the numerical calculations are obtained by combining Eq. (8) with Eqs. (50) and (51) of WWI.¹⁹

D. Computational methodology

The set of $(i_{\max} \times j_{\max} - 3)$ kinetics equations given by Eq. (3) are solved subject to the following boundary conditions. First, the monomer concentrations of the two species, N_A and N_B , are held constant. Second, the values of $f(i_{\max}, j, t)$ and $f(i, j_{\max}, t)$ are projected based on the values at $f(i_{\max} - 1, j, t - 1)$, $f(i_{\max} - 2, j, t - 1)$ and $f(i, j_{\max} - 1, t - 1)$, $f(i, j_{\max} - 2, t - 1)$, respectively. The former boundary condition is not too restrictive for the initial monomer concentrations, nucleation rates, and length of integration required before the steady state nucleation rate is reached. The latter boundary condition is slightly different from the Szilard²⁵ condition, $f(i_{\max}, j, t) = f(i, j_{\max}, t) = 0$, but its only effect is to help stabilize the numerical scheme by making the transition at the outer boundary less abrupt, in effect mimicking a larger grid. The initial concentrations of clusters containing more than one molecule are zero, i.e., $f(i, j, 0) = 0$ for $i + j > 1$.

We use an integration subroutine based on the Bulirsch-Stoer method to solve the kinetics equations.²⁶ This algorithm calculates the result at the end of a user-specified time step, Δt , by breaking the interval into finer and finer sub-intervals and extrapolating the integrated results to zero step-size. The program keeps track of the local truncation error and adjusts the internal step size to keep errors below the desired accuracy, ϵ . We use a double precision version of the subroutine with $\epsilon = 10^{-16}$. The total integration time, which ranges from 1–100 μs , is divided logarithmically into 20 time steps. The nucleation rate, as defined below, is printed out after each time step. Other intermediate quantities, such as the cluster concentrations and the values of J_A and J_B for each cluster composition, are stored after every second time step. We varied the number of time steps by factors of 2 to demonstrate that this did not affect the final nucleation rates.

The grid size and shape are chosen to provide the best balance between the number of equations that must be solved to obtain an accurate steady state solution and the time required to obtain the solution. We use the location of the

analytical saddle point as a guide to our initial choice of the grid size. However, two-dimensional plots of the steady state fluxes superimposed on the free energy surface, such as those presented later, are a very sensitive way to spot any grid related problems. If the grid is too small, unphysical flux behavior, such as flow back into the grid from outside of the computational domain, is apparent. We also spot-checked results by increasing the grid size and recalculating the solution. Although the Bulirsch–Stoer method is not the most appropriate nor the most efficient for stiff ordinary differential equations, it proved to be quite robust because of our use of double precision and the very small value of ϵ .

To avoid any ambiguity inherent in a commercial vector plotting subroutine, we wrote our own program to generate the plots of the fluxes on the free energy surfaces. Each arrow in a flux plot represents the vector sum of the locally averaged J_A and J_B . The local averages were calculated as

$$\bar{J}_A(i,j) = \frac{1}{8} \sum_{k=i-1}^i \sum_{l=j-1}^{j+1} (2 - |j-l|) J_A(k,l) \quad (9a)$$

and

$$\bar{J}_B(i,j) = \frac{1}{8} \sum_{k=i-1}^{i+1} \sum_{l=j-1}^j (2 - |i-k|) J_B(k,l), \quad (9b)$$

for $i = 1, 3, 5, \dots$ and $j = 1, 3, 5, \dots$. For the special case $i = j = 1$, these formulas need to be modified since there are then only five independent fluxes to average over.

E. Numerical and analytical nucleation rates

In a binary system, the most comprehensive way to evaluate the nucleation rate is by summing all of the fluxes, J_A and J_B , that cross any arbitrary line joining the A axis to the B axis. This procedure was first explicitly employed by Temkin and Shevelev,⁵ although a similar idea was essential in getting the correct transition from binary to unary nucleation in the continuous treatment based on the saddle point assumption.¹³ At steady state, this value for the rate must be a constant, although the transient particle formation rate will depend on the particular line chosen.²⁷ For convenience we have chosen to follow Temkin and Shevelev⁵ and use lines containing equal numbers of molecules. For lines too close to the “origin” there can be some numerical difficulties associated with taking the difference of very large forward and backward rates in Eqs. (1) and (2) to derive the smaller values of the total fluxes J_A and J_B . This effect is, however, strictly a numerical artifact associated with the finite number of digits stored, even in double precision, and not a physical one. It does not affect the fluxes farther out in the grid where the forward and backward rates are much smaller.

The nucleation rate expressions we have chosen to compare our results with are due to Reiss,⁶ Stauffer,⁷ and Wilemski.¹³ Other expressions for the binary nucleation rate have been developed using different analytical approaches by Trinkaus,²⁸ Shi and Seinfeld,²⁹ Zitserman and Berezhkovskii,³⁰ and Wu.²⁷ These either give equivalent results to the Stauffer expression or are not in forms that are readily implemented for quantitative use. Strictly, we are only using the formal rate expressions derived by Reiss and

Stauffer and not the original formulas involving the specific binary distribution given by Eq. (4). All of our quantitative results are based on our new binary SCC distribution given by Eq. (5). This is important to note because, as illustrated in WWI, there are substantial quantitative differences between the rates calculated with these two distributions. Because we have also modified the usual forms of the monomer impingement rates as well as the equilibrium number distribution, some additional changes are required in the analytical rate expressions before quantitative comparisons between the numerical solutions and analytical expressions are valid.

Both the Reiss and Stauffer rate expressions assume that the main nucleation current passes through the saddle point. All of the quantities appearing in the subsequent formulas should be understood to be evaluated at the saddle point composition. For emphasis, some of these will also be denoted with a superscript $*$. We also denote the three second derivatives of $W(i,j)$ at the saddle point as W_{AA} , W_{AB} , and W_{BB} . The Reiss theory assumes that the major flux follows the path of steepest descent across the free energy surface, and the nucleation rate expression is given by

$$J_R = D^* (p/q)^{1/2} N(i^*, j^*), \quad (10a)$$

where

$$D^* = \frac{\Gamma_A(i^*, j^*) \Gamma_B(i^*, j^*) N_A N_B}{\Gamma_A(i^*, j^*) N_A \sin^2 \theta + \Gamma_B(i^*, j^*) N_B \cos^2 \theta}, \quad (10b)$$

$$-p = W_{AA} \cos^2 \theta + 2 W_{AB} \cos \theta \sin \theta + W_{BB} \sin^2 \theta, \quad (10c)$$

$$q = W_{AA} \sin^2 \theta - 2 W_{AB} \cos \theta \sin \theta + W_{BB} \cos^2 \theta, \quad (10d)$$

$$2 \tan \theta = (W_{BB} - W_{AA}) / W_{AB} + [(W_{BB} - W_{AA})^2 / W_{AB}^2 + 4]^{1/2}. \quad (10e)$$

The rate expression of Wilemski equals that of Reiss multiplied by a prefactor that assures a smooth transition between binary and unary nucleation. The result is

$$J_{WR} = J_R \left(\frac{\nu_+ (\Delta l_+)}{2 \Delta l_+} \operatorname{erf} [\Delta l_+ [q / (2kT)]^{1/2}] + \frac{\nu_- (\Delta l_-)}{2 \Delta l_-} \operatorname{erf} [\Delta l_- [q / (2kT)]^{1/2}] \right), \quad (11)$$

where Δl_+ , Δl_- , and ν_{\pm} are defined in Eqs. (A7)–(A9) of Appendix A with $\psi = \theta$. This version of the prefactor is more general than that presented previously.¹³ Away from either axis, its value usually approaches unity. Appendix A contains a derivation of this prefactor.

The expression due to Stauffer differs from that of Reiss because it allows the direction of growth in the saddle region to be modified by the impingement rates of A and B monomers. The nucleation rate is

$$J_S = R_{av} Z N(i^*, j^*), \quad (12a)$$

where

$$R_{av} = \frac{\Gamma_A(i^*, j^*) \Gamma_B(i^*, j^*) N_A N_B}{\Gamma_A(i^*, j^*) N_A \sin^2 \phi + \Gamma_B(i^*, j^*) N_B \cos^2 \phi} \quad (12b)$$

and

$$Z = -(W_{AA} \cos^2 \phi + 2W_{AB} \cos \phi \sin \phi + W_{BB} \sin^2 \phi) / (W_{AB}^2 - W_{AA}W_{BB})^{1/2}, \quad (12c)$$

where the angle ϕ is calculated from

$$\tan \phi = s + \sqrt{s^2 + 1/\chi}, \quad (12d)$$

with the ratio of impingement rates defined as

$$\chi = \frac{\Gamma_A(i^*, j^*) N_A}{\Gamma_B(i^*, j^*) N_B} \quad (12e)$$

and

$$2s = (W_{BB}/\chi - W_{AA})/W_{AB}. \quad (12f)$$

Note that χ is the inverse of the parameter r defined by Stauffer. Finally, the combination of Stauffer's rate expression and Wilemski's prefactor gives

$$J_{\text{WS}} = J_S \left(\frac{\nu_+(\Delta l_+)}{2\Delta l_+} \operatorname{erf} [\Delta l_+ [w/(2kT)]^{1/2}] + \frac{\nu_-(\Delta l_-)}{2\Delta l_-} \operatorname{erf} [\Delta l_- [w/(2kT)]^{1/2}] \right), \quad (13a)$$

where

$$w = (W_{AA}W_{BB} - W_{AB}^2) / (W_{AA} \cos^2 \phi + 2W_{AB} \cos \phi \sin \phi + W_{BB} \sin^2 \phi), \quad (13b)$$

and where Eqs. (A7)–(A9) still apply but with $\psi = \phi$.

To provide a direct comparison with our numerical results, the location of the saddle point must be evaluated using the *thermodynamically inconsistent* Kelvin equations³¹ that include the surface tension derivatives. Any numerical scheme, such as ours, that calculates the reversible work required for cluster formation based on the overall composition of the cluster rather than the internal composition of the cluster is, in effect, ignoring surface enrichment. We note in passing that any numerical scheme that searches the free energy surface described by Eq. (6) for the saddle point also ignores surface enrichment.

The effect of using our modified distribution function, rather than the usual Eq. (4), is to increase the nucleation rate by a factor of

$$\frac{(N_A^\infty)^{x_A^*} (N_B^\infty)^{x_B^*} \exp(x_A^* \Theta_A + x_B^* \Theta_B)}{(N_A + N_B)}, \quad (14)$$

which is equivalent to the $S^{-1} \exp(\Theta)$ term in SCC theory¹⁸ for unary systems (often a factor of 10^2 to 10^4). Our use of Eq. (8) rather than Eq. (7) to calculate the impingement rates increases the kinetic prefactor of the Reiss and Stauffer formulas by a factor of 2–3. The direction of growth changes by less than 1% due to the difference in the impingement rate expressions. In the limit of unary nucleation, the rate is calculated using either Eq. (11) or (13) or the self-consistent expression given by

$$J_{\text{SCC}} = v \left(\frac{2\sigma}{\pi m} \right)^{1/2} N_1^\infty N_1 R^* \exp(\Theta [1 - \frac{1}{3}(g^*)^{2/3}]), \quad (15a)$$

where

$$R^* = (1 + 1/g^{*1/3})^2 (1 + 1/g^*)^{1/2}, \quad (15b)$$

v is the molecular volume, g^* is the number of monomers in the critical nucleus, and R^* accounts for the change due to our definition of the impingement rates. Equation (10) or (12) cannot be used to calculate unary rates because they vanish as either N_A or N_B approaches zero.

F. Binary systems considered

For our calculations we have considered two ideal systems, two systems that exhibit negative deviations from ideality, and two systems that exhibit positive deviations. The ideal systems were o-xylene–m-xylene and ethanol–hexanol, while the negative deviators were dichloromethane–tetrahydrofuran and chloroform–tetrahydrofuran. More interesting negative deviators, such as acid–water systems were not investigated because we did not wish to address the difficulties associated with surface enrichment in this paper. Choosing the positively deviating systems was difficult because we wanted to work close to the bulk miscibility limit, but not enter a regime where bulk phase separation occurs. For real systems, low temperature liquid phase data are sparse, and extrapolations from different sets of high temperature activity and heat of mixing data often give conflicting results. As a first step we therefore chose to look at positively deviating pairs that had all the properties of the highly ideal systems, o-xylene–m-xylene and ethanol–hexanol, but had excess Gibbs free energies of mixing given by the simple regular solution expression

$$g^E = Ax_A x_B. \quad (16)$$

We will refer to these systems as PD1 and PD2, respectively. Although PD1 and PD2 are not real, their behavior is representative of systems such as hydrocarbon–alcohol mixtures, for example, ethanol–hexene. Working with these two model systems has the additional advantage that direct comparisons between the ideal and partially miscible states is straightforward, and a wide range of liquid phase nonideality can be investigated by systematically varying the value of A . By setting the value of $A/(RT) = 2$, each system is at its upper critical solution temperature (UCST) and at the edge of the bulk miscibility gap; any increase in $A/(RT)$ would produce two bulk solution phases.

The physical properties of the binary mixtures and the conditions of the simulations are summarized in Appendix B. Binary nucleation has been studied experimentally for o-xylene–m-xylene and ethanol–hexanol. For these systems the simulations were done at the experimental temperature. For the other systems, temperatures were chosen which gave pure liquid vapor pressures on the order of 10 Torr. Activity behavior at higher temperatures was extrapolated to the simulation temperature by using heat of mixing data at the closest available temperature. When data were not available for surface tension or molar volume as functions of composition, we assumed the value was the mole fraction weighted average of the pure component values. The vapor compositions used in the calculations are reported in terms of the gas phase activities a_A and a_B defined as

$$a_A = N_A / N_A^\infty, \quad (17a)$$

$$a_B = N_B / N_B^\infty. \quad (17b)$$

III. RESULTS AND DISCUSSION

A. Binary nucleation through a saddle

For unary nucleation we know that when the transient birth and death equations are properly posed and solved, they give the correct theoretical steady state results.³² Thus, in the limit of nucleation of a single component, our numerical scheme must produce steady state results that agree closely with analytical theory. For binary nucleation the situation is more complex because many paths can contribute to the overall nucleation rate. When these paths are channeled through a saddle region, we would anticipate that the numerical steady state rate should agree reasonably well with either the Stauffer or Reiss theories. Flow through a saddle, however, is not the only possibility. Depending on the shape of the free energy surface and the sizes of the impingement rates, it is also possible that most of the current bypasses the saddle point. Several papers^{5,7,8,27–30,33} have discussed and analyzed this situation, and under these conditions the saddle point treatment is not adequate. For ideal gaseous and liquid mixtures whose components have similar thermodynamic and transport properties, however, there is little reason to expect disagreement between the numerical rates and the predictions of an appropriate version of binary nucleation theory using the saddle point treatment. Indeed, in modeling crystal nucleation in binary glasses, Greer *et al.*⁸ found excellent agreement with the Reiss theory when the molecular mobilities, i.e., impingement rates of the crystallizing species, were identical and poor agreement when they were not. An important issue to address, then, is over what range of impingement rates and to what extent of mixture nonideality will the saddle point treatment continue to provide reliable predictions of the nucleation rate for vapor–liquid systems.

Figures 1(a) through 1(f) compare the numerically derived nucleation rates (filled squares) for the six systems investigated with the analytical results based on J_{WS} (solid lines) and J_{WR} (dashed lines). Far from the unary limit these are generally equivalent to J_S and J_R , respectively, but an important exception is discussed below. The agreement between the numerical results and either theory is excellent for all systems in which the equilibrium vapor pressures of the pure liquids are not too dissimilar. The results illustrated in Figs. 1(a), 1(c), 1(d), and 1(e) cover ideal and both types of nonideal mixture behavior over a wide range of impingement rate ratios, yet differences between the values of J_{WS} and J_{WR} do not exceed 50%. When they do differ, it is often hard to distinguish between them on the scale of these figures, but J_{WR} lies below J_{WS} . The numerical rates and the theoretical predictions using J_{WS} are usually within 20% of each other. In the ethanol–hexanol calculations [Fig. 1(b)] the two theories agree at low ethanol activities, but at higher ethanol activities we can begin to distinguish between the Reiss and Stauffer formulations. The Reiss formulation can be low by up to an order of magnitude for the range of conditions we examined. It is worth noting that because of the great dispar-

ity in the equilibrium vapor pressures of ethanol and hexanol, all of the binary rate curves in this figure are calculated for ethanol rich conditions. Even for $a_E=0.5$ and $a_H=14$, the ethanol vapor concentration is about eight times that of hexanol ($N_E/N_H=8$), and the ethanol impingement rate is about twelve times that of hexanol ($\chi=12$). Figure 1(f) also shows conditions for which J_{WS} differs significantly from J_{WR} for the model nonideal system based on ethanol and hexanol. The figure also contains a region where both approaches differ noticeably from the numerical results. This will be discussed extensively in Sec. III B.

It is important to note that the impingement rate ratio χ is not the principal determining factor for the differences between J_{WR} and J_{WS} . In both of the ideal systems we considered, χ varies over many orders of magnitude, yet the o-xylene–m-xylene system never displays any significant differences between the predictions of the Reiss and Stauffer theories while the ethanol–hexanol system does. To be more precise, for the o-xylene–m-xylene system the Reiss and Stauffer angles never differ by more than 10° and the Stauffer rate is never more than 10% larger than the Reiss value. The differences in angle and rate in the ethanol–hexanol system can be much larger as the ethanol activity increases. To illustrate why J_{WR} and J_{WS} can differ in the ethanol–hexanol system, Figs. 2(a) through 2(c) show how the steady state nucleation fluxes behave as conditions are changed from low to high ethanol activities. In these figures, the fluxes are superimposed on a contour plot of the free energy surface calculated using Eq. (6).³⁴ The ethanol-to-hexanol impingement rate ratios (χ) for Figs. 2(a), 2(b), and 2(c) are 12, 56, and 141, respectively. In all cases the largest fluxes pass through the saddle region. For low ethanol activities, as in Fig. 2(a), there is a large free energy barrier for growth in the ethanol direction. Thus, the major flux continues down the path of steepest descent, consistent with the assumptions in the Reiss formulation despite the relatively high value of χ . In Fig. 2(b), with $\chi=56$ and the saddle point far removed from either axis, the difference between the direction of steepest descent and the principal growth direction is important, and the flux begins to deviate from the path of steepest descent. Finally, in Fig. 2(c), with $\chi=141$, the saddle point remains sufficiently far from the ethanol axis so that the difference between the growth and steepest descent directions can still be large.

The differences between the two ideal systems are due to the intrinsic properties of the free energy surface on which nucleation is occurring. In particular, the location of the saddle point plays an important role. In the o-xylene–m-xylene system, the equilibrium vapor pressures of the pure components are nearly equal, and either a very large or very small value of χ forces the saddle point to lie very close to one of the pure component axes. Near an axis no significant difference between steepest descent and growth directions is possible. In the ethanol–hexanol system, the great difference in the equilibrium vapor pressures means that it is possible to have large values of the ethanol-to-hexanol impingement rate ratio while the component activities remain roughly comparable. This places the saddle point at a reasonable distance from either pure component axis and provides enough

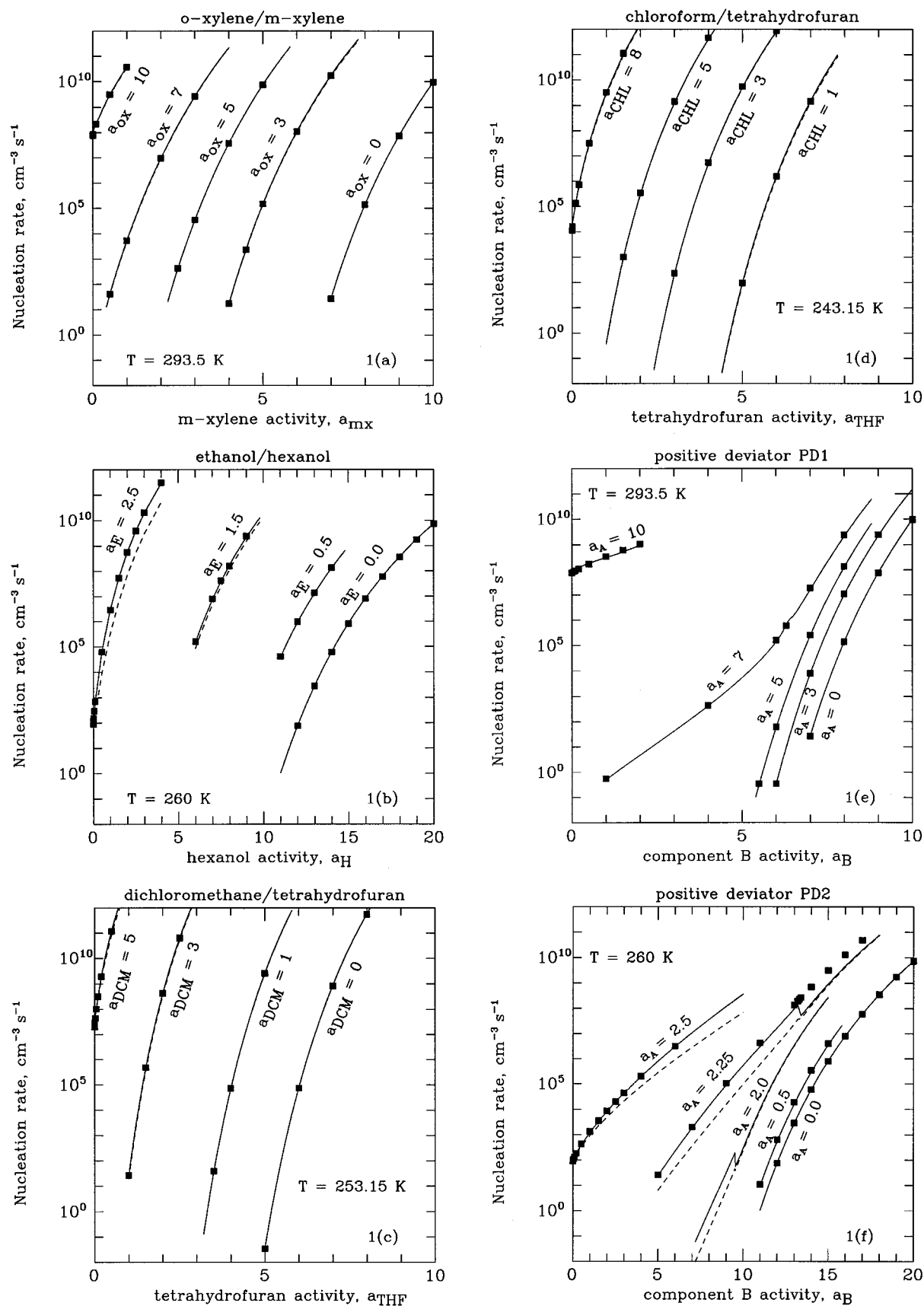


FIG. 1. Numerical nucleation rates (filled squares) are compared to the analytical predictions of J_{WS} (solid lines) and J_{WR} (dashed lines). Both analytical predictions are always plotted but the results are often indistinguishable. (a) o-xylene–m-xylene; (b) ethanol–hexanol; (c) dichloromethane–tetrahydrofuran; (d) chloroform–tetrahydrofuran; (e) the model positively deviating system based on ethanol(A)–hexanol(B); (f) the model positively deviating system based on ethanol(A)–hexanol(B). Ridge crossing is observed for $a_{\text{A}}=2.25$, $a_{\text{B}}>13$. The analytical results for $a_{\text{A}}=2.0$ are included to indicate another region ($a_{\text{B}}\geq 9.6$) where ridge crossing behavior is expected.

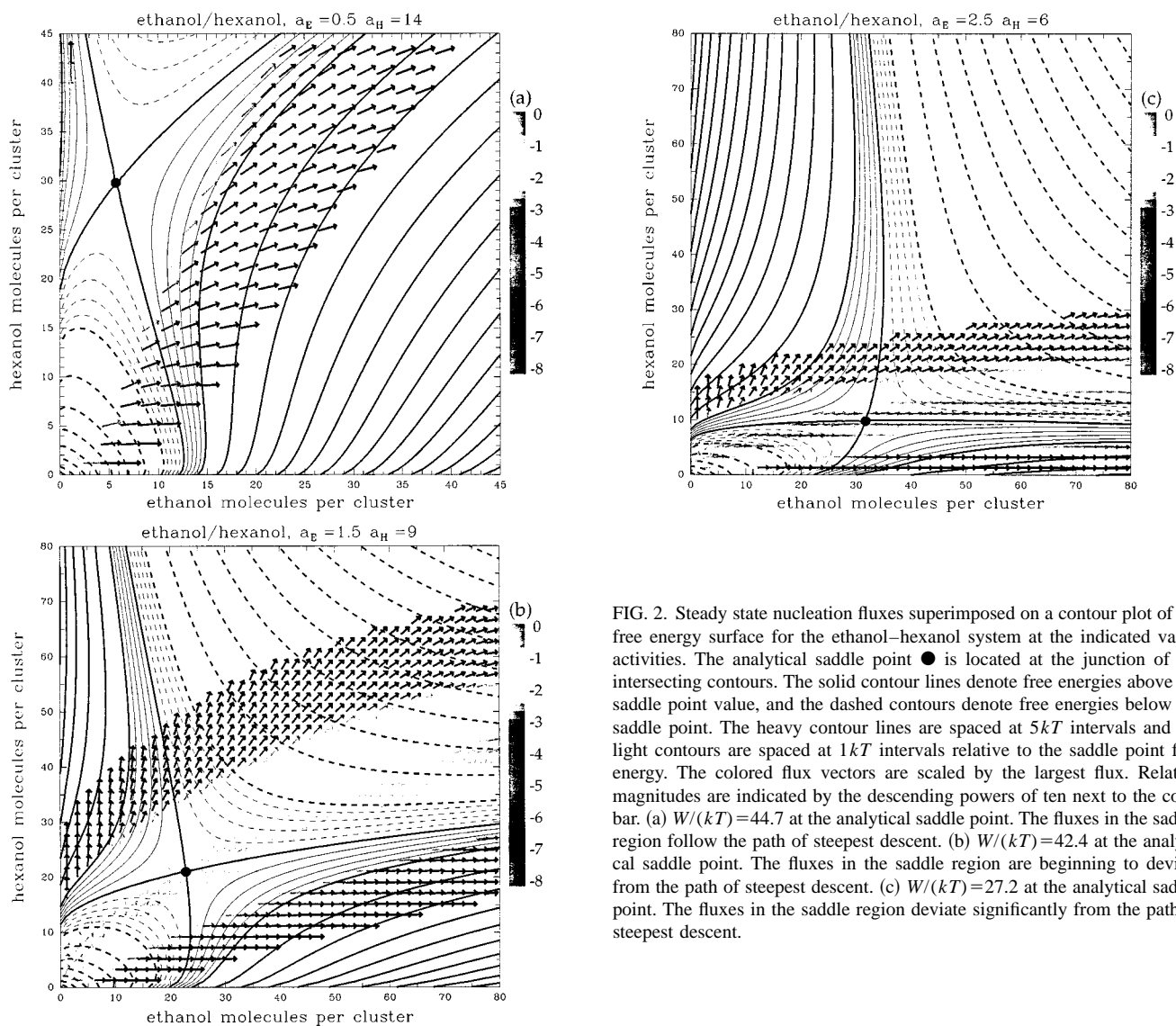


FIG. 2. Steady state nucleation fluxes superimposed on a contour plot of the free energy surface for the ethanol-hexanol system at the indicated vapor activities. The analytical saddle point \bullet is located at the junction of the intersecting contours. The solid contour lines denote free energies above the saddle point value, and the dashed contours denote free energies below the saddle point. The heavy contour lines are spaced at $5kT$ intervals and the light contours are spaced at $1kT$ intervals relative to the saddle point free energy. The colored flux vectors are scaled by the largest flux. Relative magnitudes are indicated by the descending powers of ten next to the color bar. (a) $W/(kT)=44.7$ at the analytical saddle point. The fluxes in the saddle region follow the path of steepest descent. (b) $W/(kT)=42.4$ at the analytical saddle point. The fluxes in the saddle region are beginning to deviate from the path of steepest descent. (c) $W/(kT)=27.2$ at the analytical saddle point. The fluxes in the saddle region deviate significantly from the path of steepest descent.

“room” in composition space for differences in the growth and steepest descent direction to arise. Returning to Fig. 1(b) and Fig. 2(c), we see that increasing the ethanol-to-hexanol impingement rate ratio by reducing a_H at constant a_E , leads to a convergence of the two rate predictions because the saddle point moves ever closer to the ethanol axis leaving essentially only one direction through the saddle. The disparity in equilibrium vapor pressures also introduces an asymmetry into this binary system in the following sense. In a truly hexanol rich state ($\chi < 1$) there would be no difference between the Stauffer and Reiss rate predictions because the saddle point would be too close to the hexanol axis to permit it. We conclude that the size of the χ factor is insufficient to predict whether or not the path of steepest descent is sufficiently different from the growth direction to distinguish between the Reiss and Stauffer theories. The location of the saddle point on the free energy surface plays an important role as well, and this is strongly affected by the relative sizes of the equilibrium vapor pressures and molecular volumes of the two pure components, as well as by the degree of non-ideality of the mixture.

Another interesting result is shown in Fig. 1(e) for the positively deviating binary system based on o-xylene-m-xylene at its bulk UCST. The nucleation rate curve at constant $a_A=7$ shows a distinct kink in the region where the vapor phase concentrations are similar. This kink occurs when a slight increase in the activity of component B causes the saddle point to abruptly move from the vicinity of the component A axis much closer to the component B axis. Despite this, the analytical nucleation rate predicted by J_{WS} is still in very good agreement with the numerical results. Figures 3(a) and 3(b) show the steady state fluxes across the free energy contour plot in the vicinity of this kink. Certainly, for the conditions $a_A=7$ and $a_B=6.3$ the saddle region is extremely broad, and a very large number of fluxes contribute to the overall steady state nucleation rate. A somewhat more well-defined path is emerging in Fig. 3(b) as a_B has increased by about 10%. Note the large shift in saddle point locations for these two figures.

The nucleation rate behavior in this unusual region is shown in more detail in Fig. 4. As a_B is varied, the saddle point composition passes very close to its value at the micro-

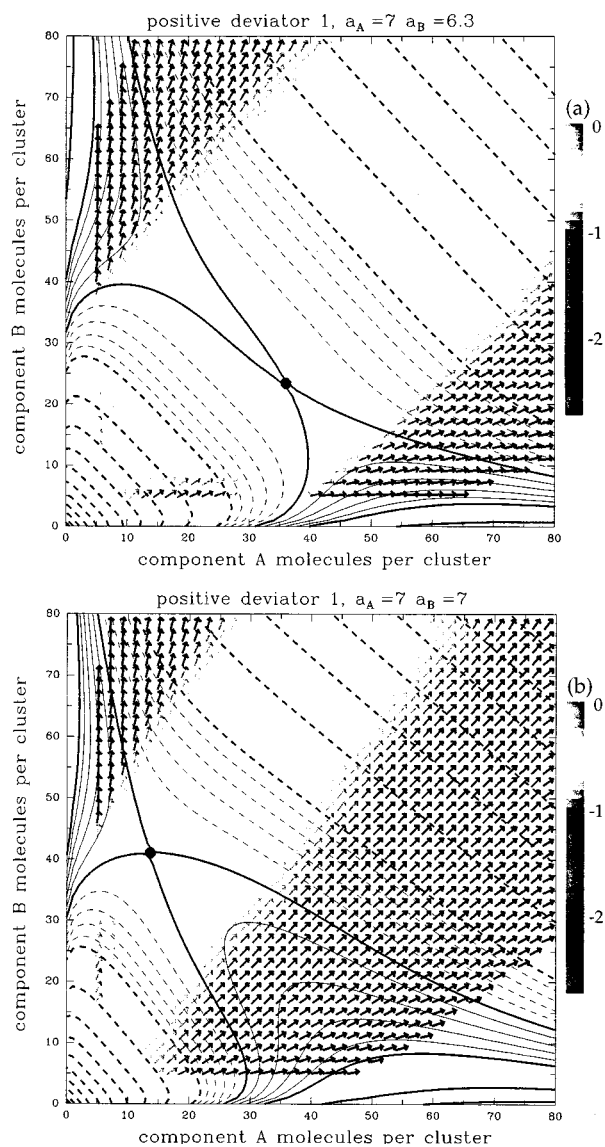


FIG. 3. Steady state nucleation fluxes superimposed on a contour plot of the free energy surface for the positively deviating system PD1 based on o-xylene(A)–m-xylene(B) at the indicated vapor activities. The saddle point location, ●, free energy contours, and flux scaling are handled as in Fig. 2. To enhance color contrast, flux vectors near the component axes are not plotted. (a) $W/(kT) = 61.5$ at the analytical saddle point. The saddle region is very broad and flat, and the flux is evenly distributed across much of the free energy surface. (b) $W/(kT) = 57.5$ at the analytical saddle point. The saddle region is still broad, but a preferred path is emerging.

scopic UCST. This causes the free energy surface to flatten and broaden and considerably reduces both the true curvature q of the free energy surface and the effective curvature parameter w in Stauffer's theory. Recall that the second and third derivatives of the free energy of mixing are zero at the bulk UCST composition. As a result, the predictions of both the Stauffer and Reiss theories become unreasonably large in this region as shown in Fig. 4 for J_S . The figure also shows that J_{WS} remains fairly well-behaved and in reasonable agreement with the numerical results, since it is designed to handle this kind of singular behavior as explained in Appendix A. Although a quadratic expansion of the free energy is insufficient when q and w equal zero, the parabolic saddle point approximation is adequately rescued by the rate pre-

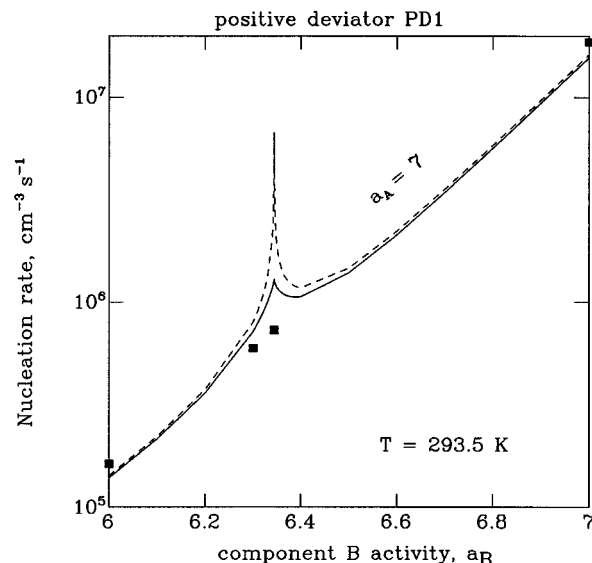


FIG. 4. Steady state nucleation rates for the positively deviating system PD1 based on o-xylene(A)–m-xylene(B) near a microscopic UCST. Numerical results (filled squares) are compared to the analytical predictions of J_{WS} (solid line) and J_S (dashed line).

scription leading to J_{WS} . Improved accuracy would probably result from a quartic expansion of the free energy, but this would further complicate the evaluation of the nucleation rate.

Except for some isolated cases that are easy to understand, our numerical results lie within 10%–20% of the predictions of Stauffer's theory when the major nucleation flux passes through the saddle. We also find very good agreement with Reiss' theory everywhere it would be expected. In this respect we affirm the conclusion of Greer *et al.*,⁸ but we conflict sharply with the results of Kožíšek and Demo,⁴ which showed no agreement with either the Reiss or Stauffer theories. On the basis of their results, Kožíšek and Demo argued that the saddle point approximation was inaccurate and that a more comprehensive rate expression was required. While we concur with their aspirations for an improved theoretical rate expression, we feel that their pessimistic conclusion about the saddle point approximation is based on an unfair comparison. In WWI we showed that uncritical use of the detailed balance expressions and the Reiss distribution for binary cluster compositions could lead to a kinetically and thermodynamically inconsistent set of evaporation rate coefficients. Numerical solution of the birth–death equations with these coefficients leads to rates that differ substantially from those predicted by Reiss' or Stauffer's analytical theories. We think this is the cause of the discrepancy found by Kožíšek and Demo. When properly constructed sets of evaporation rate coefficients are used, numerical results can be fully consistent with the appropriate analytical theory as demonstrated by our results, those of Greer *et al.*,⁸ McGraw,⁹ and those of Kožíšek and Demo⁴ for the Kelvin model of Temkin and Shevelev.⁵

B. Binary nucleation via ridge crossing

Figure 1(f) shows the nucleation rate calculations for the PD2 system, based on ethanol–hexanol, at its bulk UCST.

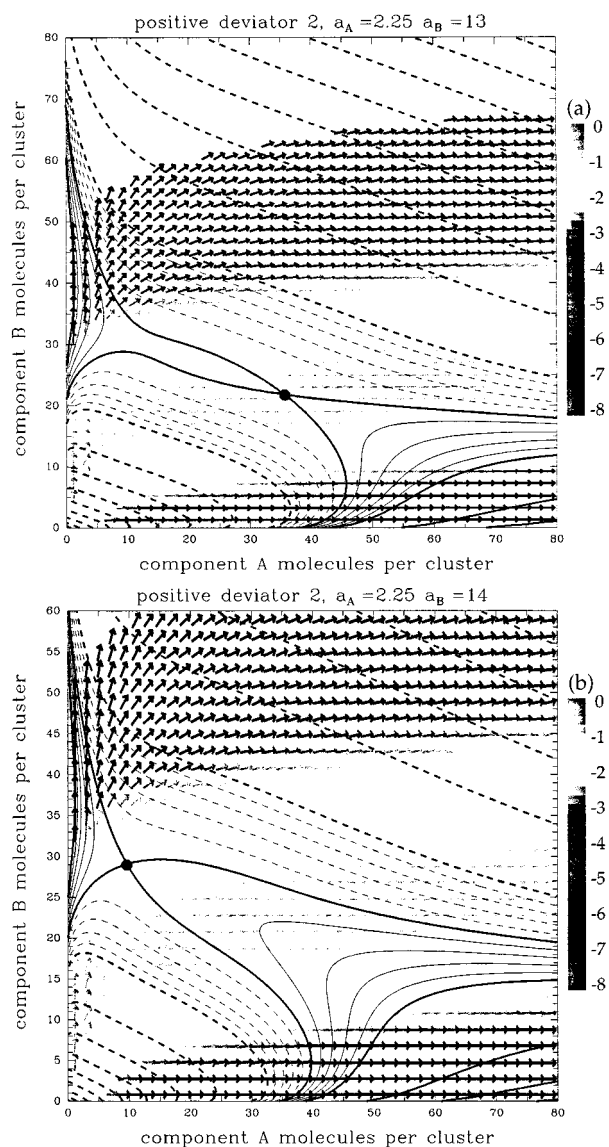


FIG. 5. Steady state nucleation fluxes superimposed on a contour plot of the free energy surface for the positively deviating system PD2 based on ethanol(A)–hexanol(B) at the indicated vapor activities. The saddle point location, ●, contour line meanings, and flux scaling are handled as in Fig. 2. The light contours are spaced at $0.5kT$ intervals relative to the saddle point. The heavy contours start at $\pm 2.5kT$ relative to the saddle and are then spaced at $5kT$ intervals. To enhance color contrast, flux vectors near the origin are not plotted. (a) $W/(kT) = 47.7$ at the analytical saddle point. The saddle region is broad and flat. The major flux flows through the saddle region in a direction distinctly different from the path of steepest descent, and the rate given by J_{WS} agrees well with the numerical result. (b) $W/(kT) = 45.5$ at the analytical saddle point. The saddle point has shifted considerably from its location in (a). The major flux now bypasses the saddle and climbs over a low ridge that extends from the saddle point toward the lower right corner. The numerical rate is 4.4 times the value given by J_{WS} .

Although J_{WS} generally agrees well with the numerical rates, there is a region where all of the saddle point theories underpredict the numerical results. These theories fail because the major flux no longer passes through the saddle, as in Fig. 5(a), but instead bends in the direction of the A axis and climbs over a rather low ridge, as in Fig. 5(b). The higher impingement rate of the A component (pseudo-ethanol) provides a kinetic boost, allowing the slightly higher free energy

barrier to be overcome. Despite this qualitative change in the rate behavior, the difference between the analytical saddle point rate and the exact numerical value is still less than a factor of 10. Until recently,³⁵ it would have been impossible to measure nucleation rates to better than a factor of 10. Formal expressions for ridge crossing rates have been derived,^{28–30} but no quantitative tests of their accuracy have been performed yet. We will defer making these quantitative comparisons until we have enough simulations of different systems to make a comprehensive assessment.

In Refs. 28–30 the occurrence of ridge crossing is ascribed to coupling between the shape of the free energy surface and a large disparity in the impingement rates ($\chi \gg 1$ or $\chi \ll 1$). None explicitly mention a factor that we have found to be important, namely, the “dynamic” behavior of the free energy surface in producing a situation favoring ridge crossing over saddle point nucleation as χ is varied. These papers leave us with the picture of a free energy surface that is fairly insensitive to changes in χ while only the behavior of the nucleation flux is influenced considerably by the size of χ . This is certainly the case in the example presented by Greer *et al.*,⁸ where χ is varied by changing the mobility of the condensed phase species without changing the free energy surface at all. Even on Trinkaus’ free energy surfaces, which pertain to the nucleation of gas bubbles in a solid matrix supersaturated with dissolved gas and lattice vacancies, the saddle point location does not appear to vary greatly with the relative concentrations of gas atoms and vacancies. By contrast, it does change considerably with the vapor composition for gas–liquid systems.

We first observed ridge crossing when we increased the activity of the lower vapor pressure species B (pseudo-hexanol) while working at a fixed activity of the high vapor pressure component A (pseudo-ethanol). For our conditions χ is about 54, but we induced ridge crossing by reducing χ , rather than by increasing it. In our example, with the impingement rate of component A fixed, an increase in the smaller impingement rate of component B causes the saddle point to shift from a location near the A component axis [Fig. 5(a)] to one much closer to the B component axis [Fig. 5(b)]. This moves it out of the path of the main nucleation current, which now flows over a gentle ridge with no significant change in direction and only a small change in location from the immediately preceding case. Thus, it is the dramatic shift in the location of the saddle point that produces ridge crossing for us. Further decreases in χ cause the saddle point to move even closer to the B axis, and eventually the main nucleation flux also shifts back to the saddle region. If we start the system in the latter condition and reverse the sequence of events by increasing χ , the first significant event is a switch of the main nucleation flux away from the saddle into a ridge crossing situation, as in Fig. 5(b). Further increases in χ , however, eventually cause the saddle point to shift abruptly to the vicinity of the A axis returning the system to a state of saddle point nucleation. This state persists as the saddle moves ever closer to the A axis until unary nucleation of component A is the dominant or only process occurring. This behavior illustrates a key point: The influence of changing impingement rates on the behavior of the nucle-

ation fluxes cannot be decoupled from the accompanying changes in the free energy surface, at least for vapor–liquid systems. At a given temperature, impingement rates are determined by the partial pressures of the two condensing species, but the same partial pressures are strongly involved in determining the shape and height of the free energy surface and the saddle point location.

The ridge crossing behavior that we observed has some interesting differences from that found by McGraw in the $\text{H}_2\text{SO}_4\text{--H}_2\text{O}$ system. There the water-to-acid impingement rate ratio χ was on the order of 10^{14} . We are able to observe ridge crossing for values of χ of only 50–100 rather than 10^{14} because the behavior of the free energy surface of the positively deviating PD2 system is very different from that of the negatively deviating acid–water system. Remember that our system is at a UCST, just at the verge of the bulk miscibility gap. Thus, the abrupt shift of the saddle point for a small change in a_B foreshadows the existence of two distinct saddle points corresponding to different critical nucleus compositions once the system is inside the miscibility gap.³⁶ In the acid–water system, the two components are always fully miscible. Thus, for the conditions studied by McGraw, the saddle point is always located near the water axis, and the primary nucleation flux eventually moves to the region between the saddle point and the water axis when χ becomes large enough. It is possible that further increases in χ will result in a transition to the unary nucleation of water in the manner implied by Shi and Seinfeld, rather than drive the system back to a state of saddle point nucleation, as in our example.

C. Transition to unary nucleation

Next we consider the transition from binary to unary nucleation. For all of the cases treated here, this transition proceeds by what we regard as the “normal” or common mechanism in which binary nucleation always occurs through the saddle. As the vapor becomes increasingly richer in one component, the saddle point approaches ever closer to the composition axis of the majority species while the binary nucleation rate steadily decreases and ultimately becomes negligible compared to the unary rate of the majority species. Temkin and Shevelev⁵ and Shi and Seinfeld²⁹ have identified other, less common mechanisms by which binary nucleation transforms into unary nucleation.

Not illustrated in Figs. 1(a)–1(f) is the fact that both J_R and J_S fail to predict the transition from binary to unary nucleation correctly. Figure 6 illustrates this clearly for the transition to pure ethanol nucleation by comparing the numerical results with J_R , J_S , and J_{WS} . For hexanol activities less than 0.01 the analytical binary rates drop below the unary rate for the expressions that do not include the prescription developed by Wilemski.¹³ Mirabel and Clavelin³⁷ suggested that the proper way to treat the transition from binary to unary nucleation was to calculate the binary rate until the number of molecules of the second component in the critical cluster drops below 1 and then to switch to the unary nucleation rate. This is not a satisfying theoretical approach. In Fig. 6 the switch would occur for $a_H < 0.09$ and would amount to an unnecessary error of up to a factor of 6.

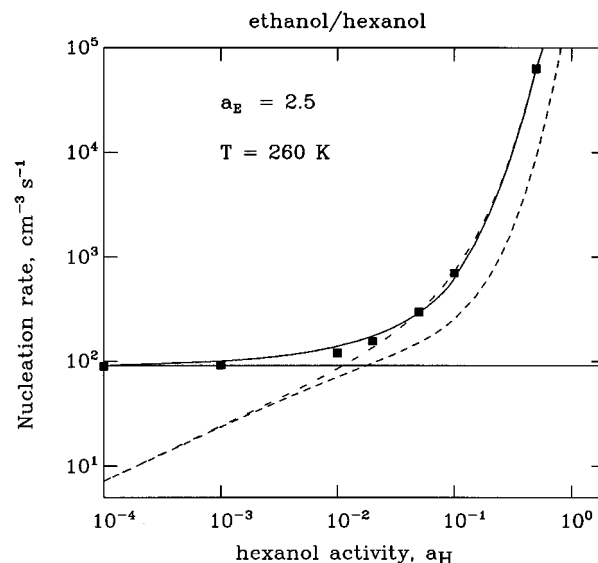


FIG. 6. Numerical steady state nucleation rates (filled squares) for the ethanol–hexanol system are compared to the analytical results given by J_{WS} (solid line), J_S (upper dashed line), and J_R (lower dashed line) for the transition from binary to pure ethanol nucleation. When $a_H < 0.09$, the number of hexanol molecules in the analytical critical nucleus drops below 1.

Less error would be incurred by simply taking the maximum or the sum of the unary and binary rates. Furthermore, an analytically derived critical nucleus composition that has slightly less than one molecule of the second species is a signal that binary nucleation is still contributing to the overall flux. Including the prefactor given by Eqs. (11) or (13) does not add much of a computational burden to the already complex binary nucleation rate calculation. Doing so enables the analytical theory to agree with the exact numerical calculations extremely well and to accommodate the singular behavior found near a microscopic UCST.

In the transition to unary nucleation discussed by Temkin and Shevelev,⁵ species *A* and *B* undergo binary nucleation at gas phase activities high enough to also allow unary nucleation of species *A*. The equilibrium vapor pressure of species *B* is then artificially reduced at fixed temperature while maintaining constant gas phase activities for both species. When the vapor pressure of species *B* is low enough, binary nucleation is precluded by slow kinetics although the saddle still exists at some distance from the *A* axis. Only unary nucleation of species *A* can then occur. Although this is an interesting mathematical procedure for forcing a transition to unary nucleation, perhaps by means of ridge crossing, we find it difficult to see how this limiting process would ever be implemented experimentally. The transition to unary nucleation analyzed by Shi and Seinfeld²⁹ does proceed through ridge crossing, but it does not involve the limiting process of Temkin and Shevelev. The ridge crossing behavior found by McGraw⁹ in the water–sulfuric acid system may be an example of this type of transition, although this needs further investigation.

IV. SUMMARY AND CONCLUSIONS

We solved the complete set of coupled differential equations describing transient binary nucleation kinetics in vapor–

to-liquid phase transitions. We investigated binary systems displaying both positive and negative deviations from ideality in the liquid phase and obtained numerical solutions over a wide range of relative rates of monomer impingement. We emphasized systems and conditions that either have been investigated experimentally or can be. For almost all of the cases we examined, we found that the major particle flux passes through the saddle point with an orientation angle that depends on the rates of monomer impingement qualitatively in accord with Stauffer's⁷ considerations. For these cases, the exact numerical steady state nucleation rates are within 10%–20% of those predicted by Stauffer's analytical theory based on the assumption of a saddle crossing. The predictions of Reiss's⁶ theory also agree with the numerical results over a wide range of relative monomer impingement rates as long as the equilibrium vapor pressures of the pure liquids are similar, but Stauffer's theory is more generally valid. Our conclusion regarding the validity of the saddle point approximation contrasts starkly with that of Kožiček and Demo.⁴ Since they studied a much simpler system than any of ours, they should have found good agreement with both Reiss' and Stauffer's theories over a fairly wide range of impingement rate ratios. We speculated that their failure to do so is most likely a consequence of using a set of evaporation coefficients that is inconsistent with the Reiss equilibrium distribution as discussed in WWI.¹⁹

In WWI we compared the experimental results of Strey and Viisanen³⁸ for ethanol–hexanol with analytical results calculated using J_{WS} , Eqs. (13), and our SCC binary distribution, Eq. (5). Although we observed an improvement in the overall fit to the data, some discrepancies remained. The excellent agreement between the numerical and analytical rate predictions for ethanol–hexanol found in the current work clearly demonstrates that this discrepancy is not due to any approximations inherent in the formulation of J_S or J_{WS} , which are equivalent nearly everywhere for this mixture. Thus, our previous calculations were, in effect, a direct comparison between experimental data and the full solution of the binary kinetics equations.

In systems that display positive deviations from ideality, the predictions of both the Stauffer and Reiss theories can become unreasonably large if either the true curvature q or effective curvature parameter w approaches zero. We observed this behavior in the PD1 system. The parabolic saddle point approximation can be adequately rescued, however, by the rate prescription outlined in Appendix A without involving higher order expansions of the free energy function.

We also found a limited range of conditions for which the major flux bypassed the saddle point and nucleation occurred by ridge crossing. Even in these cases, the analytical saddle point rate was within a factor of 10 of the numerical result. Greer *et al.*⁸ observed similar behavior for binary nucleation in the condensed phase by progressively lowering the mobility of one species. Another example of ridge crossing nucleation was reported recently by McGraw⁹ for water–sulfuric acid, a mixture that shows extremely negative deviations from ideality. In this example the ridge crossing rate exceeded the saddle point rate by three orders of magnitude, but ridge crossing was found only under conditions of ex-

tremely low sulfuric acid vapor activity that are just barely attainable experimentally. Our ridge crossing example is for a positively deviating system under conditions of relatively modest vapor activities. Although our system is hypothetical, it is similar to many real systems. This suggests that the systematic experimental study of ridge crossing nucleation is possible under readily accessible conditions.

We also studied the transition from binary to unary nucleation by progressively lowering the vapor concentration of one component. We demonstrated the previously known^{13,37} failure of both Reiss' and Stauffer's rate expressions under these conditions. The proposed remedy of Mirabel and Clavelin³⁷ was also found to be inadequate. We found that the exact numerical rates were described best by a modified version of the prescription previously proposed by Wilemski.¹³

Our results illustrate the importance of a factor that has not been properly appreciated in earlier work: the response of the free energy surface to changes in the vapor partial pressures and, therefore, in the impingement rates. The kinetic influence of the impingement rates on the nucleation path has received considerable prior attention,^{5,7,8,28–30,33,37,39} as has the shape or anisotropy of the free energy surface,^{28–30} but these factors are usually discussed as if they were independent. While this may be appropriate for transitions in condensed phase systems, for vapor-to-liquid transitions the only practical way to make large changes in the impingement rates is by varying the concentrations of the condensible species. Since these concentrations, or partial pressures, directly affect both the shape of the free energy surface and the saddle point location, all three factors work together to determine how nucleation occurs. A very large or small value of χ by itself is *not* sufficient to produce significant differences between the Stauffer and Reiss rate expressions or to induce ridge crossing. Since the location of the saddle point can be very sensitive to changes in χ , the thermodynamic properties of the mixture must also allow the saddle point composition to differ nontrivially from that of a pure critical nucleus when $\chi \ll 1$ or $\chi \gg 1$ before the main nucleation flux can deviate markedly from either the saddle point or the path of steepest descent. For many fluid systems, including non-ideal ones, these conditions cannot be attained. Furthermore, the abrupt shifting of the saddle point location for small changes in the vapor composition can be instrumental in initiating or terminating ridge crossing nucleation in mixtures with strong positive deviations from ideality. Finally, the saddle point behavior also affects the transition from binary to unary nucleation. While ridge crossing nucleation may lead to unary nucleation,²⁹ in most cases this transition occurs as a result of the saddle point merging into a pure component axis as either $\chi \rightarrow 0$ or $\chi \rightarrow \infty$.

ACKNOWLEDGMENTS

We thank Dr. C. S. Kochanek for advice on the computational work and D. Adams for help with preparing the figures. We also thank Dr. R. McGraw for sending us a preprint of his work. At Physical Sciences Inc., this work was supported by the U. S. Department of Energy, Office of Basic Energy Sciences, Division of Geosciences and Engineering

under Grant No. DE-FG02-92ER14257. Part of this work was also performed under the auspices of the U. S. Department of Energy by the Lawrence Livermore National Laboratory under Contract No. W-7405-ENG-48.

APPENDIX A: MODIFIED BINARY RATE PRESCRIPTION

In either Reiss' or Stauffer's theory, the nucleation rate is ultimately defined as

$$J = \int_{-\infty}^{+\infty} I(\xi) d\xi, \quad (\text{A1})$$

where the flux I through the saddle is approximately given by

$$I(\xi) = B^* \sqrt{P/(2\pi kT)} N(i^*, j^*) \exp[-Q\xi^2/(2kT)]. \quad (\text{A2})$$

The rotated coordinate ξ measures distance from the saddle point along an axis orthogonal to the principal flux direction. The remaining quantities are defined as

$$B^* = \frac{\Gamma_A(i^*, j^*) \Gamma_B(i^*, j^*) N_A N_B}{\Gamma_A(i^*, j^*) N_A \sin^2 \psi + \Gamma_B(i^*, j^*) N_B \cos^2 \psi}, \quad (\text{A3})$$

$$-P = W_{AA} \cos^2 \psi + 2W_{AB} \cos \psi \sin \psi + W_{BB} \sin^2 \psi, \quad (\text{A4})$$

where the angle ψ equals either θ [Eq. (10e)] or ϕ [Eq. (12d)], and Q equals either q [Eq. (10d)] or w [Eq. (13b)] depending on whether the Reiss or Stauffer rate expression is being used. See the earlier definitions for explicit expressions. The $W_{\alpha\beta}$ are the second derivatives of the free energy of cluster formation evaluated at the saddle point.

The original motivation¹³ for modifying this definition of the nucleation rate in a binary system stemmed from the recognition that the free energy surface behaved pathologically as the binary system underwent a "normal" transition (cf. Sec. III C) to a unary system by elimination of one of the condensible components from the vapor. In this case, the thermodynamic ingredients of the free energy surface always cause the curvature of the surface orthogonal to the principal nucleation flux to diverge as one component disappears. Simultaneously, the saddle point approaches ever closer to the size axis of the remaining component, and only a single nucleation path remains viable, that of unary nucleation. In mathematical terms $Q \rightarrow \infty$, the Taylor series expansion of the free energy is no longer justified, and the integral defining the rate vanishes because $I(\xi)$ is nonzero only at a single point. To overcome this deficiency, Wilemski redefined the rate as

$$J = \frac{\nu(\Delta l)}{2\Delta l} \int_{-\Delta l}^{\Delta l} I(\xi) d\xi, \quad (\text{A5})$$

where Δl was the distance from the saddle point to the nearest pure component axis and ν was the number of fluxes contributing to the total nucleation current in the interval $(-\Delta l, \Delta l)$. As the saddle point approaches a pure component axis, we find that $\Delta l \rightarrow 0$, and the above expression acts as a delta function to single out the unary rate. A more detailed explanation is available in the original paper.

Our numerical results show that the original expression gives reasonable agreement but is a bit too abrupt in changing from binary to unary nucleation, so we offer the following obvious generalization to remedy this. This new prescription allows for asymmetry in the range of integration to either side of the saddle point. The modified rate definition reads

$$J = \frac{\nu_-(\Delta l_-)}{\Delta l_-} \int_{-\Delta l_-}^0 I(\xi) d\xi + \frac{\nu_+(\Delta l_+)}{\Delta l_+} \int_0^{\Delta l_+} I(\xi) d\xi, \quad (\text{A6})$$

where Δl_- and Δl_+ , are the distances from the saddle point to each pure component axis,

$$\Delta l_+ = \frac{j^*}{\cos \psi}, \quad (\text{A7})$$

$$\Delta l_- = \frac{i^*}{\sin \psi}, \quad (\text{A8})$$

and ν_- and ν_+ count the number of currents in each half-range of integration,

$$\nu_{\pm}(\Delta l_{\pm}) = \max(1, \Delta l_{\pm}). \quad (\text{A9})$$

Equation (A6) can be rewritten as

$$J = J(\psi) \left(\frac{\nu_+(\Delta l_+)}{2\Delta l_+} \operatorname{erf} [\Delta l_+ [Q/(2kT)]^{1/2}] + \frac{\nu_-(\Delta l_-)}{2\Delta l_-} \operatorname{erf} [\Delta l_- [Q/(2kT)]^{1/2}] \right), \quad (\text{A10})$$

where

$$J(\psi) = B^* \sqrt{P/Q} N(i^*, j^*). \quad (\text{A11})$$

For rate computations, the error function is evaluated using a simple rational approximation.⁴⁰ Depending on how ψ and Q are evaluated, $J(\psi)$ is equal to either the usual Reiss⁶ or Stauffer⁷ expression. Equation (A10) resembles a result published recently by Wu,²⁷ but his expression is lacking the additional factors of $\nu(\Delta l)/\Delta l$ that are needed to obtain the proper transition to unary nucleation. The additional factor multiplying $J(\psi)$ in Eq. (A10) is almost always negligibly different from unity in which case Eq. (A10) reduces to the usual Reiss or Stauffer expressions. Only when one of the error function arguments is small does the modification factor become important.

One possibility for this is when $Q \rightarrow 0$, as mentioned by Wu.²⁷ In this case, provided $i^* > \sin \psi$ and $j^* > \cos \psi$, the limiting value of Eq. (A10) is

$$J = B^* \sqrt{P/(8\pi kT)} N(i^*, j^*) \left(\frac{i^*}{\sin \psi} + \frac{j^*}{\cos \psi} \right). \quad (\text{A12})$$

Physically, a very small value of Q corresponds to a flattening of the free energy surface in the saddle region. The most likely possibility for observing this type of behavior is for conditions that put the binary system very close to a microscopic UCST without actually giving rise to a second saddle point.³⁶ An example of this type was discussed in Sec. III A for the positively deviating PD1 system based on o-xylene-m-xylene. This type of behavior occurs only under very spe-

cial circumstances. The much more common situation is when one of the Δl 's is approaching zero as a component's vapor concentration is reduced. Under these conditions, a transition to unary nucleation is expected.

To see how Eq. (A10) works for this case, we consider the limit in which $N_B \rightarrow 0$. In this limit we also find that $j^* \rightarrow 0$, $\psi \rightarrow 0$, $\Delta l_+ \rightarrow 0$, $\Delta l_- \rightarrow \infty$, $Q \rightarrow \infty$, $\Delta l_+ Q^{1/2} \rightarrow 0$, $\nu_- = \Delta l_-$, and $\nu_+ = 1$. With these limiting values, we can simplify Eq. (A10) to read

$$J = B^* \left(\frac{P}{Q} \right)^{1/2} N(i^*, j^*) \left[\left(\frac{Q}{2\pi kT} \right)^{1/2} + \frac{1}{2} \right]. \quad (\text{A13})$$

The two bracketed terms are the limits of the respective two terms in Eq. (A10). The $Q^{1/2}$ term, which was present in the original version,¹³ gives rise to the exact unary nucleation rate by cancelling the corresponding factor in the denominator of $J(\psi)$. The other term, $\frac{1}{2}$, is new, and it represents a declining contribution of binary nucleation to the total rate, making the transition to purely unary nucleation less abrupt.

APPENDIX B: PHYSICAL PROPERTY DATA

This appendix contains the physical property data for the pure components and binary mixtures used in the exact numerical calculations. For all cases, except ethanol–hexanol, the surface tension, σ (dynes/cm), and molecular volumes of the mixtures were assumed to be linear functions of the molar concentration. The temperature used in the calculation is denoted $T_s(K)$, ρ is density (g/cm^3), P is pressure (Torr or Pa as noted), g^E is the excess Gibb's free energy of mixing (J/mol), and $H(x)$ is the heat of mixing (J/mol). The parameter x_B is the mole fraction of the second species and $x_A = 1 - x_B$.

1. Ideal systems

(i) o-xylene–m-xylene: The data are from Mirabel and Katz⁴¹ and Katz *et al.*⁴² with a correction for a misprint in the formula for $\rho_{\text{o-xylene}}$:

$$T_s = 293.15 \text{ K},$$

$$M_{\text{o-xylene}} = M_{\text{m-xylene}} = 106.16,$$

$$\rho_{\text{o-xylene}} = 1.1101 - 0.6063(10^{-3})T - 0.1389(10^{-5})T^2 + 0.39376(10^{-8})T^3 + 0.43423(10^{-11})T^4,$$

$$\rho_{\text{m-xylene}} = 1.0506 - 0.10251(10^{-3})T - 0.34865(10^{-5})T^2 + 0.77487(10^{-8})T^3 - 0.70068(10^{-11})T^4,$$

$$\log_{10}(P_{\text{o-xylene}}^\infty) = 6.99891 - 1474.679/(T - 59.464),$$

P in Torr,

$$\log_{10}(P_{\text{m-xylene}}^\infty) = 7.00908 - 1462.27/(T - 58.055),$$

P in Torr,

$$\sigma_{\text{o-xylene}} = 32.51 - 0.1101(T - 273.15),$$

$$\sigma_{\text{m-xylene}} = 31.23 - 0.1104(T - 273.15).$$

(ii) Ethanol–hexanol: The property data for this mixture are all at 260 K and have been taken from Strey and Viisanen:³⁸

$$T_s = 260 \text{ K},$$

$$M_{\text{ethanol}} = 46.07, \quad M_{\text{hexanol}} = 102.17,$$

$$\rho_{\text{ethanol}} = 0.8175,$$

$$\rho_{\text{hexanol}} = 0.8454,$$

$$P_{\text{ethanol}}^\infty = 598.36 \text{ Pa},$$

$$P_{\text{hexanol}}^\infty = 2.643 \text{ Pa},$$

$$\sigma(x_B) = 25.02 + 7.31088x_B - 3.43199x_B^2.$$

2. Nonideal systems

(i) Dichloromethane (DCM)–tetrahydrofuran (THF): The density fits are derived from data in the *Solvent Safety Handbook*.⁴³ The vapor pressure fits are from *Lange's Handbook of Chemistry*.⁴⁴ The surface tension fit for DCM is also from *Lange's Handbook of Chemistry*⁴⁴ while the surface tension behavior of THF is estimated, based on a reported value of $\sigma = 26.5$ at 298 K and an estimated slope of 0.1 dyne/(cm K). The nonideality of the mixture was parametrized by Byer *et al.*⁴⁵ The heat of mixing parametrization is from the *Handbook of Heats of Mixing*.⁴⁶

$$T_s = 253.15 \text{ K},$$

$$M_{\text{DCM}} = 84.93, \quad M_{\text{THF}} = 72.10,$$

$$\rho_{\text{DCM}} = 1.3608 - 1.8(10^{-3})(T - 273.15),$$

$$\rho_{\text{THF}} = 0.9109 - 1.1(10^{-3})(T - 273.15),$$

$$\log_{10}(P_{\text{DCM}}^\infty) = 7.4092 - 1325.9/(T - 20.55), \quad P \text{ in Torr},$$

$$\log_{10}(P_{\text{THF}}^\infty) = 6.99515 - 1202.29/(T - 46.9), \quad P \text{ in Torr},$$

$$\sigma_{\text{DCM}} = 30.41 - 0.1284(T - 273.15),$$

$$\sigma_{\text{THF}} = 29.0 - 0.1(T - 273.15),$$

$$g^E/(x_A x_B) = Ax_B + Bx_A - Dx_A x_B; \quad A = -0.92241,$$

$$B = -0.87287, \quad D = 0.22232 \text{ at } T = 305.15 \text{ K},$$

$$H(x_B) = x_B(1 - x_B)[-5387.9 - 1040.6(1 - x_B) + 2240.2(1 - x_B)^2] \text{ at } T = 305.15 \text{ K}.$$

(ii) Chloroform (CHL)–tetrahydrofuran (THF): The density fit is derived from data in the *Solvent Safety Handbook*.⁴³ The vapor pressure and surface tension fits are from *Lange's Handbook of Chemistry*.⁴⁴ The nonideality of the mixture was parametrized by Byer *et al.*⁴⁵ The heat of mixing parametrization is from the *Handbook of Heats of Mixing*.⁴⁶

$$T_s = 243.15 \text{ K},$$

$$M_{\text{CHL}} = 119.37,$$

$$\rho_{\text{CHL}} = 1.526\,43 - 1.8563(10^{-3})(T - 273.15) \\ - 0.5309(10^{-6})(T - 273.15)^2 \\ - 8.81(10^{-9})(T - 273.15)^3,$$

$$\log_{10}(P_{\text{CHL}}^{\infty}) = 6.4934 - 929.44/(T - 77.12), \quad P \text{ in Torr,}$$

$$\sigma_{\text{CHL}} = 29.91 - 0.1295(T - 273.15),$$

$$g^E/(x_A x_B) = A x_B + B x_A - D x_A x_B; \quad A = -1.393\,52,$$

$$B = -1.580\,92, \quad D = 0.586\,06 \quad \text{at } T = 305.15 \text{ K,}$$

$$H(x_B) = x_B(1 - x_B)[-8019.2 - 11\,312.4(1 - x_B) \\ + 9423.9(1 - x_B)^2] \quad \text{at } T = 294.05 \text{ K.}$$

(iii) o-xylene–m-xylene positive deviator (PD1): The physical properties of this system are identical to o-xylene–m-xylene, but the free energy of mixing is adjusted to put the mixture on the verge of partial miscibility:

$$T_s = 293.15 \text{ K,}$$

$$g^E/(x_A x_B) = A = 2RT_s.$$

(iv) Ethanol–hexanol positive deviator (PD2): The physical properties of this system are identical to ethanol–hexanol, but the free energy of mixing is adjusted to put the mixture on the verge of partial miscibility:

$$T_s = 260 \text{ K,}$$

$$g^E/(x_A x_B) = A = 2RT_s.$$

¹K. F. Kelton, *J. Non-Cryst. Solids* **163**, 283 (1993).

²B. E. Wyslouzil and J. H. Seinfeld, *J. Chem. Phys.* **97**, 2661 (1992).

³K. Nishioka and K. Fujita, *J. Chem. Phys.* **100**, 532 (1994).

⁴Z. Kožíšek and P. Demo, *J. Cryst. Growth* **132**, 491 (1993); *Mater. Sci. Eng. A* **173**, 45 (1993).

⁵D. E. Temkin and V. V. Shevelev, *J. Cryst. Growth* **66**, 380 (1984).

⁶H. Reiss, *J. Chem. Phys.* **18**, 840 (1950).

⁷D. Stauffer, *J. Aerosol Sci.* **7**, 319 (1976).

⁸A. L. Greer, P. V. Evans, R. G. Hamerton, D. K. Shangguan, and K. F. Kelton, *J. Cryst. Growth* **99**, 38 (1990).

⁹R. McGraw, *J. Chem. Phys.* **102**, 2098 (1995).

¹⁰W. J. Shugard, R. H. Heist and H. Reiss, *J. Chem. Phys.* **61**, 5298 (1974).

¹¹H. Vehkamäki, P. Paatero, M. Kulmala, and A. Laaksonen, *J. Chem. Phys.* **101**, 9997 (1994).

¹²B. Wyslouzil and G. Wilemski (in preparation).

¹³G. Wilemski, *J. Chem. Phys.* **62**, 3763 (1975).

¹⁴G. Wilemski, *J. Phys. Chem.* **91**, 2492 (1987).

¹⁵C. Flageollet-Daniel, J. P. Garnier, and P. Mirabel, *J. Chem. Phys.* **78**, 2600 (1983).

¹⁶A. Laaksonen and M. Kulmala, *J. Chem. Phys.* **95**, 71 (1991).

¹⁷C. L. Weakliem and H. Reiss, *J. Phys. Chem.* **98**, 6408 (1994); G. Wilemski, *J. Chem. Phys.* (this issue) **103**, 1119 (1995).

¹⁸L. Gershick and C.-P. Chiu, *J. Chem. Phys.* **93**, 1273 (1990).

¹⁹G. Wilemski and B. E. Wyslouzil, *J. Chem. Phys.* (preceding paper) **103**, 1127 (1995).

²⁰J. L. Katz, see Ref. 9 in Ref. 13.

²¹M. Kulmala, A. Laaksonen, and S. L. Gershick, *J. Aerosol Sci.* **23**, 309 (1992).

²²X. C. Zeng and D. W. Oxtoby, *J. Chem. Phys.* **95**, 5940 (1991).

²³C. L. Weakliem and H. Reiss, *J. Chem. Phys.* **99**, 5374 (1993).

²⁴A. Jaeger-Voirol and P. Mirabel, *J. Phys. Chem.* **92**, 3518 (1987).

²⁵As discussed by W. J. Dunning, in *Chemistry of the Solid State*, edited by W. E. Garner (Academic, New York, 1955), p. 159; and in *Nucleation*, edited by A. C. Zettlemoyer (Marcel Dekker, New York, 1969), p. 1.

²⁶W. H. Press, B. P. Flannery, S. A. Teukolsky, and W. T. Vetterling, *Numerical Recipes: The Art of Scientific Computing* (Cambridge University Press, Cambridge, England, 1985).

²⁷D. T. Wu, *J. Chem. Phys.* **99**, 1990 (1993).

²⁸H. Trinkaus, *Phys. Rev. B* **27**, 7372 (1983).

²⁹G. Shi and J. H. Seinfeld, *J. Chem. Phys.* **93**, 9033 (1990).

³⁰V. Yu. Zitserman and L. M. Berezhkovskii, *J. Colloid Interface Sci.* **140**, 373 (1990).

³¹M. Kahlweit, *Z. Phys. Chem. (Frankfurt)* **34**, 251 (1962); G. Wilemski, *J. Chem. Phys.* **88**, 5134 (1988).

³²F. F. Abraham, *J. Chem. Phys.* **51**, 1632 (1969).

³³D. Stauffer and C. S. Kiang, *Icarus* **21**, 129 (1974).

³⁴In plotting Figs. 2, 3, and 5 we use Eq. (6) simply because it is the most familiar form of the free energy surface based on the capillarity approximation. The new composition dependent factors in Eq. (5) represent additional contributions to the reversible work of cluster formation. One way to account for these changes in a dimensionally consistent fashion is by modifying Eq. (6) to read $W'(i,j) = W(i,j) + kT(x_A \Theta_A + x_B \Theta_B) + x_B kT \ln(N_B^{\infty}/N_A^{\infty})$. The geometrical effect of including the new composition dependent factors is that of adding a tilted plane to the free energy surface described by $W(i,j)$. For the systems we examined, the features of the two free energy surfaces are essentially the same, and the choice of free energy surface does not affect the conclusions we draw from Figs. 2, 3, and 5. We also confirmed that the analytical nucleation rates calculated using the appropriate derivatives based on W' agree to within 3% of those calculated using W .

³⁵R. Strey, P. Wagner, and Y. Viisanen, *J. Phys. Chem.* **98**, 7748 (1994).

³⁶A. K. Ray, M. Chalam, and L. K. Peters, *J. Chem. Phys.* **85**, 2161 (1986).

³⁷P. Mirabel and J. L. Clavelin, *J. Aerosol Sci.* **9**, 219 (1978).

³⁸R. Strey and Y. Viisanen, *J. Chem. Phys.* **99**, 4693 (1993).

³⁹V. Raghavan and M. Cohen, *Acta Metall.* **20**, 779 (1972); *Scr. Metall.* **7**, 591 (1973).

⁴⁰Equation (7.1.25) in *Handbook of Mathematical Functions*, edited by M. Abramowitz and I. A. Stegun (U. S. Government Printing Office, Washington, DC, 1972).

⁴¹P. Mirabel and J. L. Katz, *J. Chem. Phys.* **67**, 1697 (1977).

⁴²J. L. Katz, C. J. Scoppa II, N. G. Kumar, and P. Mirabel, *J. Chem. Phys.* **62**, 448 (1975).

⁴³*Solvents Safety Handbook*, edited by D. J. De Renzo (Noyes Data Corporation, Park Ridge, NJ, 1986).

⁴⁴J. A. Dean, *Lange's Handbook of Chemistry and Physics*, 14th edition (McGraw-Hill, New York, 1972).

⁴⁵S. M. Byer, R. E. Gibbs, and H. C. Van Ness, *AIChE J.* **19**, 244 (1973).

⁴⁶J. J. Christensen, R. W. Hanks, and R. M. Izatt, *Handbook of Heats of Mixing*, Vol. I and Supplement to Vol. I (Wiley, New York, 1982).